

## Search for galactic axions with a traveling wave parametric amplifier

R. Di Vora, A. Lombardi, A. Ortolan, R. Pengo, and G. Ruoso<sup>✉\*</sup>  
*INFN, Laboratori Nazionali di Legnaro, 35020 Legnaro (Padova), Italy*

C. Braggio  
*INFN, Sezione di Padova, 35100 Padova, Italy*  
*and Dipartimento di Fisica e Astronomia, 35100 Padova, Italy*

G. Carugno and L. Taffarello  
*INFN, Sezione di Padova, I-35100 Padova, Italy*

G. Cappelli, N. Crescini, M. Esposito,<sup>†</sup> L. Planat, A. Ranadive, and N. Roch  
*Université Grenoble Alpes, CNRS, Grenoble INP, Institut Néel, 38000 Grenoble, France*

D. Alesini, D. Babusci, A. D'Elia, D. Di Gioacchino, C. Gatti, C. Ligi, G. Maccarrone, A. Rettaroli, and S. Tocci  
*INFN, Laboratori Nazionali di Frascati, 00044 Frascati (Roma), Italy*

D. D'Agostino, U. Gambardella, and G. Iannone  
*Dipartimento di Fisica E. R. Caianiello, 84084 Fisciano (Salerno), Italy*  
*and INFN, Sezione di Napoli, 80126 Napoli, Italy*

P. Falferi  
*Istituto di Fotonica e Nanotecnologie, CNR Fondazione Bruno Kessler, I-38123 Povo, Trento, Italy*  
*and INFN, TIFPA, 38123 Povo (Trento), Italy*

(QUAX Collaboration)

 (Received 19 April 2023; accepted 3 August 2023; published 27 September 2023)

A traveling wave parametric amplifier has been integrated in the haloscope of the QUAX experiment. A search for dark matter axions has been performed with a high- $Q$  dielectric cavity immersed in an 8 T magnetic field and read by a detection chain having a system noise temperature of about 2.1 K at the frequency of 10.353 GHz. Scanning has been conducted by varying the cavity frequency using sapphire rods immersed into the cavity. At multiple operating frequencies, the sensitivity of the instrument was at the level of viable axion models.

DOI: [10.1103/PhysRevD.108.062005](https://doi.org/10.1103/PhysRevD.108.062005)

### I. INTRODUCTION

The axion is a hypothetical particle that arises from the spontaneous breaking of the Peccei-Quinn symmetry of quantum chromodynamics (QCD), introduced to solve the so-called strong  $CP$  problem [1–3]. It is a pseudoscalar

neutral particle having negligible interaction with the ordinary matter, making it a favorable candidate as a main component of dark matter [4–6]. Cosmological and astrophysical considerations suggest an axion mass range  $1 \mu\text{eV} < m_a < 10 \text{ meV}$  [7].

The hunt for axions is now world spread, and most of the experiments involved in this search use detectors based on the haloscope design proposed by Sikivie [8,9]. Among them are ADMX [10–13], HAYSTAC [14–16], ORGAN [17,18], CAPP-8T [19,20], CAPP-9T [21], CAPP-PACE [22], CAPP-18T [23], CAST-CAPP [24], CAPP-12TB [25], GrAHal [26], RADES [27–29], TASEH [30], QUAX [31–36], and KLASH [37,38]. Dielectric and plasma haloscopes have also been proposed, the most notable examples being MADMAX [39,40] and ALPHA [41,42],

\*Corresponding author: [Giuseppe.Ruoso@lnl.infn.it](mailto:Giuseppe.Ruoso@lnl.infn.it)

<sup>†</sup>Present address: CNR-SPIN Complesso di Monte S. Angelo, 80126 Napoli, Italy.

*Published by the American Physical Society under the terms of the Creative Commons Attribution 4.0 International license. Further distribution of this work must maintain attribution to the author(s) and the published article's title, journal citation, and DOI. Funded by SCOAP<sup>3</sup>.*

respectively. The haloscope concept is based on the immersion of a resonant cavity in a strong magnetic field in order to stimulate the inverse Primakoff effect, converting an axion into an observable photon [43]. To maximize the power of the converted axion, the cavity resonance frequency has to be tuned to match the axion mass, while larger cavity quality factors  $Q$  will result in larger signals. Different solutions have been adopted to maximize the signal-to-noise ratio, facing the problem from different angles. Resonant cavities of superconductive and dielectric materials are becoming increasingly popular because of their high  $Q$  [44–47]. In this work, we describe the results achieved by the haloscope of the QUAX-*ax* experiment, based on a high- $Q$  dielectric cavity immersed in a static magnetic field of 8 T. Cooling of the cavity at  $\sim 100$  mK reduces thermal fluctuations and enables operation of a traveling wave parametric amplifier (TWPA) at about the quantum limit. This is the first example of a high-frequency haloscope (above 10 GHz) instrumented with a near-quantum-limited wideband amplifier. A key step in the realization of an apparatus capable of searching for dark matter axions over an extended mass region. Section II describes the experimental setup with the characterization of all the relevant components, while in Sec. III details in the data analysis procedure are given. Since no dark matter signals have been detected, in the same section upper limits for the axion-photon coupling are deduced.

## II. EXPERIMENTAL SETUP

### A. General description

The core of the haloscope is a high- $Q$  microwave resonant cavity: At a temperature of about 4 K and under a magnetic field of 8 T, we measured an internal quality factor of more than  $9 \times 10^6$  [48]. It is based on a right-circular cylindrical copper cavity with hollow sapphire cylinders that confine higher-order modes around the cylinder axis. The useful mode is a TM<sub>030</sub> one, which has an effective volume for axion searches [8,9] of  $3.4 \times 10^{-2}$  liters at the resonant frequency of 10.353 GHz. Cavity tuning is obtained by displacing triplets of 2-mm-diameter sapphire rods relative to the top and bottom cavity end caps. Independent motion of the two triplets is obtained by mechanical feedthroughs controlled by a room temperature motorized linear positioner. An extensive description of the cavity design and properties can be found in Ref. [48].

The layout of the measurement setup is shown in Fig. 1. The microwave cavity is immersed in an 8 T magnetic field generated by a superconducting solenoid, and it is read by a tunable dipole antenna with coupling  $\beta$ . The antenna is the inner core of a superconducting rf cable, for which the final dielectric insulation and metallic shielding have been removed for a length of 12 mm. The antenna position is determined by a spring placed between the cavity top and

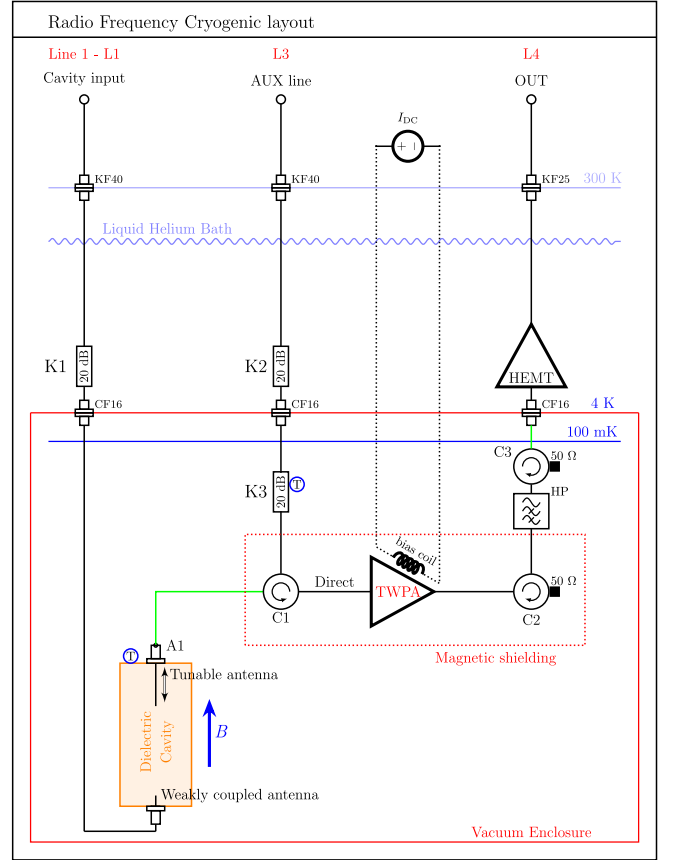


FIG. 1. Schematics of the experimental apparatus. The microwave cavity (orange) is immersed in the uniform magnetic field  $B$  generated by the magnet. C1, C2, and C3 are circulators, and HP is an 8 GHz high-pass filter. K1, K2, and K3 are attenuators, shown with their reduction factor in decibels. The components kept in the high vacuum region are enclosed in a red box. Circled T are RuO thermometers. KF40 and KF25 are rf feedthroughs with ISO-KF 40 and ISO-KF 25 flanges, respectively. CF16 are rf feedthroughs with ConFlat 16 flange. Superconducting NbTi rf cables are in green. Details on the components are given in Appendix B.

the outside of the rf cable and acting against an electrical motorized linear drive placed at room temperature and connected with a thin steel wire. Precise positioning with an electronic controller is possible over a length of about 20 mm, that allows for  $\beta$  values in the range 2–20. Because of tight mechanical constraints, the cavity works only in the overcoupled regime. A weakly coupled port (coupling about 0.01) is used for calibration purposes and is connected to the room temperature electronics by means of line L1. Cabling losses and the use of the attenuator K1 (20 dB) ensure an attenuation of about 30 dB for thermal power inputs from room temperature.

The tunable antenna output is fed onto a circulator (C1) using a superconducting NbTi cable. C1 is directly connected to the input of a TWPA [49], which serves as preamplifier of the system detection chain. Further

amplification at a cryogenic stage is done using a low-noise high-electron-mobility transistor (HEMT) amplifier. In order to avoid backaction noise from the HEMT, a pair of isolators (C2 and C3) and an 8 GHz high-pass filter are inserted between the TWPA and the HEMT. The output of the cryogenic HEMT is then delivered to the room temperature electronics using line L4. The auxiliary line L3 is used for calibrations and to provide a pump signal to the TWPA: It is connected to the line L4 by means of the circulator C1, and 20 + 20 dB of attenuation prevents thermal leakage from room temperature components and from the bath at 4 K. Finally, a dc current source is connected to a superconducting coil used to bias the TWPA. Following Fig. 1, all components within the red box “Vacuum Enclosure” are thermally anchored at the mixing chamber of a dilution unit and enclosed in a vacuum chamber immersed in a liquid helium Dewar. Two ruthenium oxide thermometers measures the temperature of the cavity and of attenuator K3, respectively.

The room temperature electronics scheme is shown in Fig. 2. Signals from line L4 are amplified by a second HEMT and split by a power divider. One of the divider two outputs is fed into a spectrum analyzer (SA), used for diagnostic and calibration. The input of the SA is referred as measurement point P4. The other output of the divider is

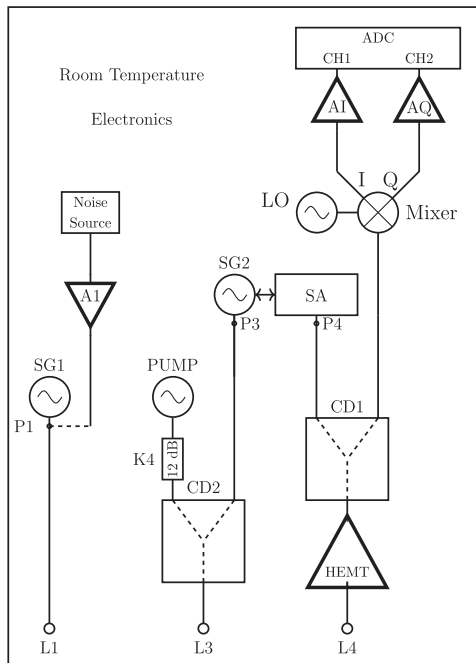


FIG. 2. Room temperature electronics. CD1 and CD2 are power splitters/combiners; LO, SG1, SG2, and PUMP are signal generators; SA is a spectrum analyzer; AI and AQ are low-frequency amplifiers; A1 is a rf amplifier; ADC is an analog to digital converter with inputs CH1 and CH2. The signal generator SG2 can be controlled by the spectrum analyzer for tracking to measure the cavity reflection spectrum. The lines L1, L3, and L4 are connected to the corresponding lines in Fig. 1.

down-converted using a mixer driven by the signal generator LO, delivering a power of 12 dBm at a frequency about 500 kHz below the cavity resonance. The room temperature chain is the same used in our previous measurements [32]: The low-frequency in-phase and quadrature outputs of the mixer are amplified and then sampled with a 2 Ms/s analog to digital converter (ADC) and stored on a computer for off-line data analysis. Data storage is done with blocks of about 4 s of sampled data for both output channels of the mixer.

By using the external source control option of the spectrum analyzer SA, it is possible to use the generator SG2 as a tracker to measure the cavity reflection spectrum S43 (input from line L3–output from line L4). The reflection spectrum provides information on the loaded quality factor  $Q_L$ , resonance frequency  $f_c$ , and coupling  $\beta$  of the tunable antenna. A diode noise source, having an equivalent noise temperature of about  $10^4$  K, can be fed to line L1 for testing after being amplified in such a way to have an equivalent noise temperature inside the microwave cavity slightly in excess of the thermodynamic temperature. A microwave signal generator and a microwave spectrum analyzer are used for the measurement of the system noise temperature as described below. All rf generators and the spectrum analyzer are frequency locked to a global positioning system disciplined reference oscillator.

### 1. Cryogenic and vacuum system

The cryogenic and vacuum system is composed of a Dewar and a  $^3\text{He}$ - $^4\text{He}$  wet dilution refrigerator. The Dewar is a cylindrical vessel of height 2300 mm, outer diameter 800 mm, and inner diameter 500 mm. The dilution refrigerator is a refurbished unit previously installed in the gravitational wave bar antenna Auriga test facility [50]. Such a dilution unit (DU) has a base temperature of 50 mK and cooling power of 1 mW at 120 mK. The DU is decoupled from the gas handling system through a large concrete block sitting on the laboratory ground via a Sylomer carpet where the Still pumping line is passing. This assembly minimizes the acoustic vibration induced on the TWPA, which is rigidly connected to the mixing chamber. Once the helium Dewar has been filled up with liquid helium, the DU column undergo a fast precooling down to liquid-helium temperatures via helium gas exchange on the inner vacuum chamber (IVC). This cooling-down operation takes almost 4 h. When a temperature of 4 K has been reached, the precooling phase ends, and the inner space of the IVC is evacuated. From that point on, the dilution refrigerator takes over, and the final cooling temperature slightly above 50 mK is attained after about 5 h. A pressure of around  $10^{-7}$  mbar was monitored without pumping on the IVC room temperature side throughout all the experimental run. Temperatures are measured with a set of different thermometers. Most of them are used to monitor the behavior of the dilution unit.

## 2. Magnet system

A NbTi superconducting solenoid provides the background field of 8 T (value at the center of the magnet), charged at a final current of 92 A with a ramp rate not exceeding 7 mA/s to reduce eddy currents losses in the ultracryogenic environment. When the current reaches the nominal value, a superconducting switch can be activated and the magnet enters the persistent mode. In this mode, the stability assures a loss of the magnetic field lower than 10 ppm/h. For this measurement campaign such mode was actually not used, and the magnet was kept connected to the current source. The magnet has an inner bore of diameter 150 mm and a length of 450 mm. When the magnet is driven by the 92 A current, the effective squared field over the cavity length amounts to  $50.8 \text{ T}^2$ .

If the magnet was not shielded, the TWPA and sensible electronics would be exposed to a stray field in the range of 0.2–0.3 T along its length, well above the operative conditions. In order to reduce the stray field in the area of the TWPA, a counterfield is locally generated by an additional superconducting solenoid, made of NbTi superconducting wire (0.8 mm diameter) wound on an aluminum reel. The inner diameter of this winding is 77.8 mm, and its height is 250 mm. The counterfield winding is biased in series to the main 8 T magnet, so it is able to reduce the field in the volume occupied by the TWPA, at any field strength, to a mean value of 0.04 T. To shield such remaining field, a hybrid box encapsulates the two circulators C1 and C2 and the TWPA. This hybrid box is constituted by an external box of lead and an internal one of CRYOPERM®. The box dimension is  $35 \times 65 \times 210 \text{ mm}^3$ , with one small base opened to allow cabling, and is thermally anchored to the DU mixing chamber.

## 3. Amplifier characterization

The TWPA (see Fig. 3) has been characterized following the procedure described in Ref. [51]. In particular, its working point in terms of bias current  $I_b$ , frequency  $f_P$ , and power  $A_P$  of the pump generator PUMP in Fig. 2 has been

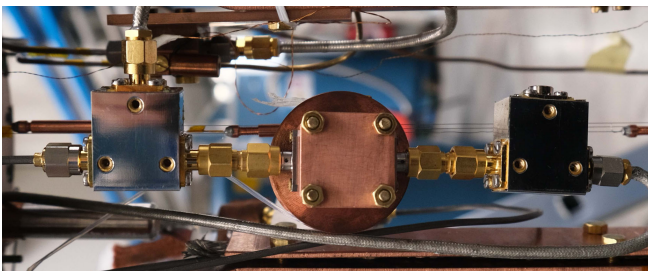


FIG. 3. Picture of the traveling wave parametric amplifier. The TWPA is enclosed in the central square box; the circle on the background is the holder of the superconducting coil providing the bias magnetic field. The two three-port boxes are isolator C2 (on the right) and circulator C1 (on the left).

chosen in order to minimize the system noise temperature  $T_{\text{sys}}$  at the cavity unshifted frequency  $\nu_c$ . The performances of the TWPA have been measured several times with the magnetic field off and then with the magnet energized once to 4 T and once to 8 T. All the resulting values of  $T_{\text{sys}}$  are compatible, around 2.0 K. During the magnet current ramp up, we monitored the wide bandwidth gain of the amplifier, to look for possible variations of the working point induced by the stray field passing through the shielding. Since no changes have been observed, one can conclude that the residual field is much below one flux quanta. The wide bandwidth gain of the amplifier is shown in Fig. 4(a). The pump frequency is set to  $f_P = 9.4181 \text{ GHz}$ , with  $A_P = -16.5 \text{ dBm}$ , and  $I_b = -1.38 \text{ mA}$ . It is evident from the figure that large (10 dB) oscillations of the gain are present at frequencies corresponding to higher gain. By precisely varying bias and pump frequency, it is possible to align a gain maximum to the cavity frequency: A gain maximum is normally equivalent to a minimum system noise temperature. Figure 4(b) shows the gain in a 4 MHz interval centered at the cavity resonant frequency. The two gain profiles are obtained with two different values of bias

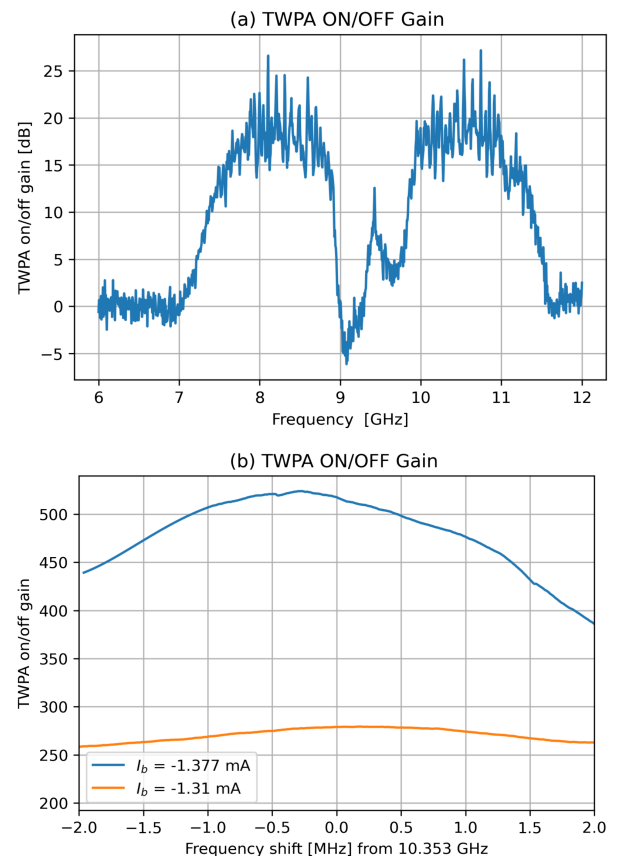


FIG. 4. Wide (a) and small (b) bandwidth gain of the traveling wave parametric amplifier. The gain has been estimated by the changes in transmission between the two cases pump on and pump off [51]. (b) The two curves have been obtained with two different values of bias  $I_b$  on the TWPA.

TABLE I. Summary of measurement of system noise temperature  $T_{\text{sys}}$  at the cavity main frequency  $\nu_c \simeq 10.353$  GHz. “Res.” stands for resonance and “Temp.” for temperature.

n	Magnetic field (T)	Cavity temp. (K)	$T_{\text{sys}}$ (K) On res.	K3 Temp. (K)	$T_{\text{sys}}$ (K) Off res.
1	0	0.12	$2.12 \pm 0.05$	0.18	$2.22 \pm 0.06$
2	0	0.12	$2.04 \pm 0.03$	0.19	$1.94 \pm 0.03$
3	4.0	0.13	$2.11 \pm 0.03$	0.22	$2.16 \pm 0.03$
4	0	0.12	$1.89 \pm 0.04$	0.18	$1.98 \pm 0.05$
5	8.0	0.11	$2.23 \pm 0.06$	0.18	$2.26 \pm 0.06$

$I_b$ : Different values of bias set different working points for the TWPA, with corresponding different gain values and profiles. In general, higher gains mean a much sharper gain profile, but even for the sharpest one a useful region of flat gain of about 1 MHz is obtained.

Table I shows the measured values of system noise temperatures, all of them measured at the test frequency  $\nu_c = 10.353$  GHz. The table shows cavity and attenuator temperatures, which contribute in different ways to the noise: The off cavity resonance value refers to a frequency 1 MHz detuned by  $\nu_c$ , where only the attenuator noise is seen by the TWPA, while on resonance a combination between cavity noise and attenuator noise forms the input noise. Only for the case of critical coupling ( $\beta = 1$ ) is the noise at the cavity frequency determined only by the cavity temperature. Except for the case  $n = 5$  (magnetic field 8 T), having  $\beta \simeq 12$ , the other measurements have  $\beta \simeq 3$ . One extra measurement has been done at the frequency  $\nu_{c,2} = 9.404061$  GHz, where another cavity mode is present. For such measurement, the pump frequency was set to  $f_{p,2} = 8$  GHz, for a resulting  $T_{\text{sys}}(\nu_{c,2}) = 2.1 \pm 0.1$  K.

For the selected cavity mode TM030, the average value is  $T_{\text{sys}}^{\text{avg}} = 2.06 \pm 0.13$  K on resonance and  $T_{\text{sys}}^{\text{avg}} = 2.07 \pm 0.14$  K off resonance. The central values come from the weighted average, while their errors are the standard deviation of all the values, showing a much wider distribution compared with the error of the single values. The resulting gain for the detection chain, from point A1 in Fig. 1 to point P4 in Fig. 2, is  $74.7 \pm 0.1$  dB. We have also obtained the gains for the other two rf lines, resulting in  $-61.3 \pm 0.1$  dB from point P1 to A1 and  $-50.9 \pm 0.1$  dB from point P3 to A1. All these gain values are those in the presence of a magnetic field at 8 T.

We can try now to evaluate all the various contributions to the measured noise level. In the quantum regime ( $k_B T \ll h\nu$ ), the number of noise photons at frequency  $\nu$  emitted by a thermal source is given by

$$N(\nu, T) = \frac{1}{2} \coth\left(\frac{h\nu}{2k_B T}\right), \quad (1)$$

where  $h$  is the Planck constant,  $k_B$  is the Boltzmann constant, and  $T$  is a thermodynamic temperature. At the considered temperatures, the noise is entirely due to quantum fluctuations, as the contribution of the thermal photons is negligible.

At a given signal frequency  $\nu_s$ , the noise power spectral density at the output of the HEMT amplifier is

$$\begin{aligned} \text{PSD}_{\text{HEMT}}(\nu_s) = & G_{\text{HEMT}}[N_{\text{HEMT}} + (1 - \Lambda_2)N_2 \\ & + \Lambda_2 G_{\text{TWPA}}(N_{\text{TWPA}} + (1 - \Lambda_1)N_1 \\ & + \Lambda_1 N(\nu_s, T_s) + \Lambda_1 N(\nu_i, T_i))]h\nu_s, \quad (2) \end{aligned}$$

where  $G_{\text{TWPA}}$  is the net gain of the TWPA and  $N_{\text{TWPA}}$  and  $N_{\text{HEMT}}$  are the added noise of the TWPA and HEMT, respectively.  $\Lambda_1 < 1$  is the transmission of the lossy chain from point A1 to the TWPA, and, analogously,  $\Lambda_2 < 1$  is the transmission from the output of the TWPA to the HEMT;  $N_1$  and  $N_2$  are the noise contributions coming from a simple beam splitter model for a lossy element.

$N(\nu_s, T_s)$  and  $N(\nu_i, T_i)$  represent the quantum noise contributions at the signal frequency equal to the cavity frequency  $\nu_s = \nu_c$  and at the idler frequency  $\nu_i = 2f_p - \nu_c$ , respectively [51]. At the idler frequency, the noise source is the attenuator K3, whose temperature is measured by one of the two thermometers. Its temperature has actually to be increased by the power leakage coming from the 4 K and room temperature stages. Considering the attenuation of K2 and K3 and cabling losses, we added 40 mK to the thermodynamic temperature of K3. At the signal frequency, the effective temperature is an intermediate value between the cavity temperature and the temperature of K3, the exact value depending on the coupling  $\beta$ : For  $\beta = 1$ , we have just the cavity temperature.

The line transmissions are estimated at room temperature for the nonsuperconducting cabling, resulting in  $\Lambda_1 \simeq -0.3$  dB and  $\Lambda_2 \simeq -0.7$  dB, which in linear units are close to 1. Such transmissions show low losses for the lines and allowed us to neglect the noise contributions  $N_1$  and  $N_2$  in Eq. (2). In addition, the high gain of the HEMT allows us to neglect all the noise contribution entering after its amplification.

With such simplifications, Eq. (2) can be recast to estimate the total system noise (referred at the point A1),

$$\text{PSD}_{\text{A1}}(\nu_s) = \frac{\text{PSD}_{\text{HEMT}}(\nu_s)}{\Lambda_1 \Lambda_2 G_{\text{TWPA}} G_{\text{HEMT}}} = N_{\text{sys}} h\nu_s, \quad (3)$$

where we have defined  $N_{\text{sys}}$  as the total number of noise photons for the system, obtaining

$$N_{\text{sys}} \simeq N(\nu_s, T_s) + N(\nu_i, T_i) + \frac{N_{\text{TWPA}}}{\Lambda_1} + \frac{N_{\text{HEMT}}}{\Lambda_1 \Lambda_2 G_{\text{TWPA}}}. \quad (4)$$

TABLE II. Noise contributions to the system noise. In the column “Value”, the noise is expressed in terms of equivalent noise temperature. The following values have been used:  $\nu_s = 10.353$  GHz,  $\nu_i = 7.94$  GHz, and the thermodynamic temperatures  $T_s = 0.16$  K and  $T_i = 0.22$  K.  $N_{\text{TWPA}}/\Lambda_1$  is the difference between the measured  $N_{\text{sys}}$  and the sum of the preceding terms.

Term	Value (K)	$N$ photons
$N(\nu_s, T_s)$	0.27	0.5
$N(\nu_i, T_i)$	0.27	0.7
$N_{\text{HEMT}}/\Lambda_1\Lambda_2G_{\text{TWPA}}$	0.39	0.8
$N_{\text{sys}}$	2.06	4.2
$N_{\text{TWPA}}/\Lambda_1$		2.2

Giving the measured value  $T_{\text{sys}} = 2.06 \pm 0.13$  K, we obtain in terms of photons a noise level:

$$N_{\text{sys}} = \frac{k_B}{h\nu_s} T_{\text{sys}} = 4.2 \pm 0.3. \quad (5)$$

In order to disentangle the contribution of the HEMT, we measured the system noise with the TWPA off (with pump off and without bias). The resulting noise temperature in this case was  $49 \pm 1$  K, with a total gain reduced by a factor 125. The contribution of the HEMT to the total noise temperature is then  $0.39 \pm 0.01$  K. Table II summarizes the noise contributions and allows one to derive the TWPA added noise as  $N_{\text{TWPA}} \simeq 2.1$  photons at the frequency of 10.353 GHz.

The measured value of  $T_{\text{sys}}$  represent a reduction of about 30% with respect to our previous realization of a TWPA-based detection chain [51]. Improvements can be ascribed to better rf cabling, better system thermalization, and the use of a different TWPA device with lower internal losses. Distributed dielectric losses in the TWPA itself are one of the primary sources of extra noise [52]. In this device, they reach values around 11 dB at 10 GHz. Despite this significant internal loss, we could demonstrate a total system noise temperature of 2.1K above 10 GHz, which, to the best of our knowledge, has never been reported before in the context of axion detection or quantum computing. More investigations will be needed to establish the maximum operation frequency of a TWPA for axion detection.

#### 4. Data taking

The search for axion dark matter has been performed over a time span of about 17 consecutive hours. The cavity antenna coupling has been set to overcritical, with the target to have a loaded quality factor about 4 times smaller than the axion one [53]. This is important for what concerns data analysis. Data taking is divided in different units that we usually call runs, each run differing from another normally for the cavity central frequency that can be varied with the sapphire triplets described above. The detection chain

TABLE III. Summary of the runs performed for the axion dark matter search. The cavity frequency is the value determined via a fast tracking spectrum on the SA. The frequency of the LO has been set to 10.353 GHz for all runs but run 404, where it is set to 10.3529 GHz.  $T_c$  and  $T_{K3}$  are the cavity and attenuator K3 temperatures, respectively.

Run n	$\nu_c$ (GHz)	Duration (s)	$T_c$ (mK)	$T_{K3}$ (mK)
389	10.353 525	2000	113	177
392	10.353 499	2000	111	178
394	10.353 473	2000	112	181
395	10.353 473	4000	113	185
397	10.353 444	2000	114	182
399	10.353 424	4800	112	177
401	10.353 399	28000	110	176
404	10.353 368	2000	110	176

system noise temperature and gain have been measured once at the beginning of the scanning session, and we monitored the time stability of the gain by injecting a rf pure tone of amplitude  $-90$  dBm on line L3 using SG2 at a frequency 900 kHz above the LO frequency. The LO frequency is chosen in order to keep the cavity frequency in a central band of the ADC working region. Each data taking step is composed of the following actions.

*Action 1.*—Set the cavity frequency to the desired value by moving the sapphire triplets. Set the LO frequency: This is actually not done for every step, since normally the change in cavity frequency is much smaller of the ADC bandwidth.

*Action 2.*—Measure a cavity reflection spectrum by tracking generator SG2 with the spectrum analyzer SA. Data are saved on a file to be fitted to deduce the antenna coupling  $\beta$ .

*Action 3.*—Measure a cavity transmission spectrum by using the noise source on line L1 and acquiring data with the ADC. Data are also taken with the spectrum analyzer SA for quick analysis. The number of 4 s blocks acquired with the ADC is normally about 30.

*Action 4.*—Measure the cavity output with all the inputs off, acquiring data with the ADC. This is the axion search data, and normally we collect 500 blocks of 4 s length each. Some runs have been done with a larger number of blocks. Again, data are also taken with the spectrum analyzer SA for quick analysis.

Table III summarizes all the scans performed. Figure 5 shows all the vacuum spectra measured with the spectrum analyzer. Such plots are taken only for control purpose, while the data sampled by the ADC and stored in the computer are those used for the search and will be discussed in Sec. III.

#### 5. Raw data processing

The 4-s-long time sequences produced by the ADC are divided into chunks about 1.5 ms long, which are Fourier

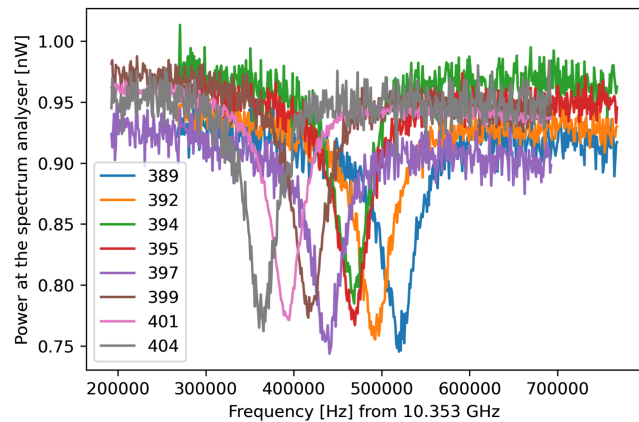


FIG. 5. Cumulative plots of the axion search measurements with the magnet energized (action 4). Such plots are taken using the spectrum analyzer, i.e., at the point P4 in Fig. 2, only for control purpose during data taking, and are not used in the data analysis. The different levels outside the resonance is a measure of the gain stability of the system, kept within a few percent in a 17 h time span. The resolution bandwidth for these plots is 1 kHz. Different colors refer to the different runs.

transformed and averaged. Another averaging is then performed to obtain a single power spectrum  $PS_n$  for each run having a resolution of  $B = 651$  Hz and covering the down-converted window  $[-1, +1]$  MHz. A raw data processing is performed to obtain relevant parameters. This is the same procedure already described in Ref. [33]. In particular, the antenna coupling  $\beta$  is obtained by fitting the cavity reflection spectrum measured with the spectrum analyzer SA with tracking generator SG2 (see “action 2”). The cavity loaded quality factor  $Q_L$  and central frequency  $\nu_c$  are obtained by fitting the average spectra obtained from the ADC data collected while the diode noise source was at the input of line L1 (see “action 3”). The resulting

TABLE IV. Summary of the parameters obtained by the fits of preliminary data for all the runs performed. Ref. peak is the amplitude of the reference peak due to the pure tone injected by SG2 on line L3 during data taking at a frequency 900 kHz above the reference oscillator of the mixer. The fit errors on the values of cavity frequencies are about 100 Hz, for the loaded quality factors about 3000, and for the  $\beta$ 's about 0.2.

Run n	$\nu_c - 10.353$ GHz (Hz)	Cavity $Q_L$	$\beta$	Ref. peak (a.u.)
389	522 600	230 000	10.9	179
392	494 100	240 000	12.0	185
394	468 800	245 000	12.2	186
395	468 800	245 000	12.2	187
397	439 800	245 000	11.4	175
399	418 500	245 000	11.4	191
401	393 100	250 000	11.4	186
404	365 400	255 000	11.9	193

parameters are reported in Table IV. The table reports also the amplitude of the reference peak set to the frequency +900 kHz in the down-converted spectra. This measurement shows again that the stability of the detection chain gain was within a few percent along the complete data taking.

During the raw analysis, a careful check of the ADC data compared with the SA data has evidenced a problem present in the down-converted data. The ADC input is filtered by a single pole low pass filter having the  $-3$  dB point at about 1.7 MHz. Unfortunately, this is not enough to avoid aliasing of the rather flat noise input. From the comparison of the high-frequency and down-converted spectra, we estimate that the measured wideband noise is about a factor 1.7 larger with respect to the real average noise in the vicinity of the cavity resonance.

Each power spectrum  $PS_n$  is the readout of the ADC input, and to obtain the power at the cavity output it must be divided by the overall gain. Alternatively, one equals the noise level measured at the ADC with the power given by the effective noise temperature of the system. We have assumed that the system noise temperature has not changed over the entire data taking time, having a duration of 17 h. Indeed, the relative error of the  $T_{\text{sys}}$ , about 6.3%, is larger than the relative changes of the reference peak as obtained by Table IV having a maximum of 5.1%. For each run we assume that the noise level at the cavity frequency is

$$P_n(\nu) = k_B T_{\text{sys}}^{\text{ADC}} B, \quad (6)$$

where  $B = 651$  Hz is the bin width,  $k_B$  is the Boltzmann constant, and  $T_{\text{sys}}^{\text{ADC}} = 1.7 \times T_{\text{sys}} = 3.5$  K.

### III. DATA ANALYSIS AND RESULTS

#### A. Axion detection procedure

Detection algorithms can be discussed in the classical “hypothesis testing” framework: On the basis of the observed data, we must decide whether to reject or fail to reject the null hypothesis (data are consistent with noise) against the alternative hypothesis (noise and signal are present in data) usually by means of a detection threshold determined by the desired significance level. The outcome of this data analysis step is a set of “axion candidate” masses or frequencies. However, axion signal has some distinctive properties that can be used to discriminate it from spurious detected signals (see Sec. III B). We emphasize that the basis of our detection algorithm is a very robust model of the noise that allows us to use maximum likelihood criterion (i.e., a  $\chi^2$  test) to implement the decision rule. Deviations from the model of the noise power spectral density are clues of excess power that could be associated with a signal. In the frequency domain, the noise model for the power spectral density at the haloscope output (under the general assumptions of linearity, stationarity,

ergodicity, and single-resonance system) is simply a first-order polynomial ratio:

$$p(\nu) = \frac{\nu - \nu_z + i\gamma_z}{\nu - \nu_p + i\gamma_p}, \quad (7)$$

where  $(\nu - \nu_{p,z} + i\gamma_{p,z})$  are the pole and the zero values in the complex plane, respectively. The fitting function to the power spectrum data, with fit parameters  $a, b, \dots, f$ , reads

$$F(\nu) = e^2 * \frac{|\nu - a + ib|^2}{|\nu - c + id|^2} + f * (\nu - c), \quad (8)$$

where the linear term accounts for the slight dependence of the ADC gain on frequency and we made the approximation  $\nu^2 - \nu_{p,z}^2 \simeq 2\nu_{p,z}(\nu - \nu_{p,z})$ . The parameter  $e$  is a normalization factor.

The estimate of power spectrum resides on the Bartlett method of averaging periodograms [54]. For every measured run in Table III, we performed the fit with  $F(\nu)$  and used the  $\chi^2$  to test the hypothesis of no signal. We discovered that the quality, i.e., the value for example of the reduced  $\chi^2$ , of the fits was worsening with the duration of the run. Indeed, a key issue is the stability of our setup, where it is actually not surprising that drifts will appear over timescales of several hours. For this reason we decided, for the analysis procedure, to split every run in subruns with a fixed length of 2000 s and to perform the fits on each of the resulting 23 subruns. For each subrun, the fits are performed on a window of 200 bins (bin width = 651 Hz) centered at the cavity peak frequency. The weight on each bin is the measured value divided by  $\sqrt{N}$ ,  $N$  is the number of averages: For a 2000 s duration and 651 Hz bin width,  $N \simeq 1.37 \times 10^6$ . The null hypothesis  $H_0$  is accepted for  $\chi^2$  probability above the chosen threshold of  $P_\alpha = 0.001$ . Since for all subruns  $H_0$  was not rejected, it is then possible to build a grand spectrum of all the residuals of the different fits, which will result in an increased sensitivity.

The grand spectrum is built by performing a weighted average of all the bins with the same frequency for all subruns residuals, again using as weight the values previously used to do the fits. The grand spectrum of the residuals and the relative histograms of the normalized values are shown in Fig. 6. The grand spectrum has 442 bins, a total  $\chi^2 = 452$  having a probability  $P_{\chi^2} = 0.37$ , and the hypothesis of data compatible with pure thermal noise is not rejected. Such a claim is done without modeling the axion. The minimum value of the sigma of the residuals in Fig. 6 is  $(6.2 \pm 0.4) \times 10^{-24}$  W, obtained at the frequency of 403645 Hz shifted from 10.353 GHz with a total integration time of 36000 s. The value expected from Dicke's radiometer equation is  $(6.5 \pm 0.4) \times 10^{-24}$  W.

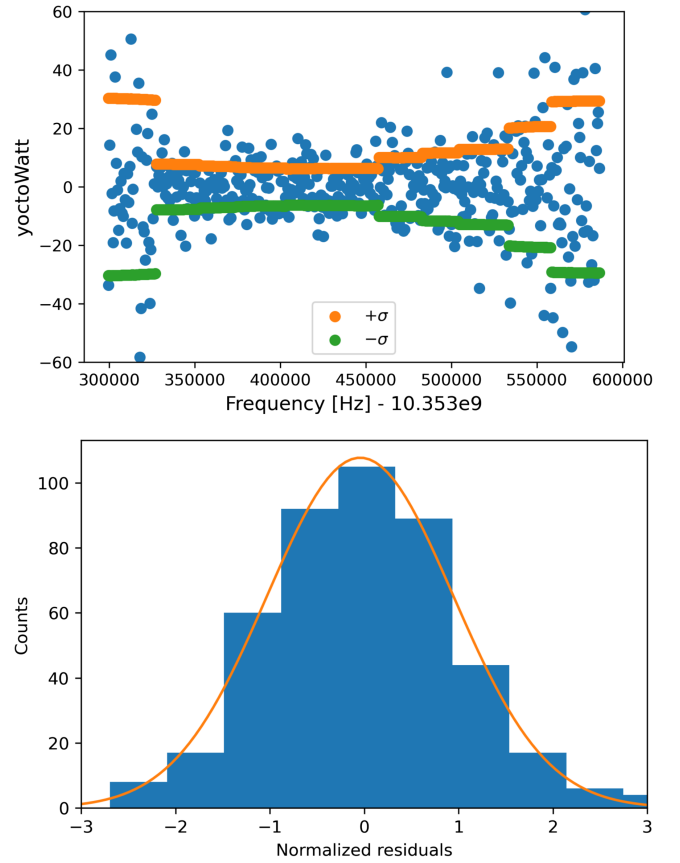


FIG. 6. Grand spectrum of the residuals. (a) Residuals and their sigma versus vs frequency. The bin size is 651 Hz. (b) Histogram of the normalized residuals. The fit function is a Gaussian function with average  $-0.04$  and width  $0.99$ .

## B. Axion discrimination procedures

Candidates that survive to a simple repetition of the  $\chi^2$  test (using a new dataset taken in the same experimental conditions) can be further discriminated using a stationarity and on-off resonance tests. A stationarity test verifies that a signal is continuously present during a data taking. An on-off resonance test verifies that the signal can be maximized by a tuning procedure of the cavity. Moreover, the dependence of signal power on the antenna coupling  $\beta$  can also be checked. Eventually, a change of the magnetic field allows us to verify if the signal power is proportional to the magnetic field squared. Candidates that passed this step would be associated to axionic dark matter. When no axion candidate survives at the sensitivity level of current axion models [55], an upper limit on axion-photon coupling can be set for the standard model of galaxy halo.

## C. Upper limits on axion-photon coupling

Having data compatible with the presence of only noise, we can then proceed to derive bounds on the coupling constant of the axion to the photon, assuming specific coupling and galactic halo models. Bounds can be inferred adopting the following approach. The power spectra for

each subrun are fitted again using as a fit function the sum of the background  $F(\nu)$  [see Eq. (8)] and the expected power produced by axion conversion for specific values of the axion mass within the measured bandwidth. By placing the axion coupling as a free parameter, since this new fit procedure returns as output the smallest possible observable power, it is possible to obtain an upper limit on the coupling constant  $g_{a\gamma\gamma}$ . Again,  $\chi^2$  probability is used to evaluate the goodness of the fit.

To calculate the expected axion signal we will rely on the standard halo model for dark matter and assume that dark matter is composed by axions in its totality. With this hypothesis, the axion energy distribution is given by a Maxwell-Boltzmann distribution [53]

$$f_a(\nu, \nu_a) = \frac{2}{\sqrt{\pi}} \sqrt{\nu - \nu_a} \left( \frac{3}{1.7\nu_a \langle \beta_a^2 \rangle} \right)^{3/2} e^{-\frac{3(\nu - \nu_a)}{1.7\nu_a \langle \beta_a^2 \rangle}}, \quad (9)$$

where  $\nu_a$  is the axion frequency and  $\langle \beta_a^2 \rangle$  is the rms of the axion velocity distribution normalized by the speed of light. The factor 1.7 takes into account that we are working in the laboratory frame [56]. The rms of the galactic halo is 270 km/s, resulting in a  $\langle \beta_a^2 \rangle$  of  $8.1 \times 10^{-7}$ .

In a haloscope, the power is released in a microwave cavity of frequency  $\nu_c$  and volume  $V$ , immersed in a static magnetic field  $B_0$ . At the antenna output, with coupling  $\beta$ , the available power is described by the spectrum

$$S_a(\nu, \nu_a, \nu_c) = g_{a\gamma\gamma}^2 \frac{\hbar^3 c^3 \rho_a}{m_a^2} \times \frac{2\pi\nu_c B_0^2 V C_{030}}{\mu_0} \frac{\beta}{1 + \beta} \cdot F_c(\nu, \nu_c) \cdot f_a(\nu, \nu_a), \quad (10)$$

where  $\rho_a \sim 0.45 \text{ GeV/cm}^3$  is the local dark matter density [57],  $g_{a\gamma\gamma}$  is the coupling constant of the axion-photon interaction, and  $m_a$  is the axion mass. The form factor  $C_{030} = 0.035$  has been recalculated to take into account the static magnetic field distribution over the cavity mode TM030 used in our haloscope. The function

$$F_c(\nu, \nu_c) = \frac{Q_L}{1 + \left[ 2Q_L \frac{(\nu - \nu_c)}{\nu_c} \right]^2} \quad (11)$$

describes the bandwidth limited amplification of the microwave cavity, with  $Q_L$  its loaded quality factor.

We split the measured frequency range in 56 intervals having center frequencies  $\nu_i$ , where we tested our sensitivity for an axion of mass  $m_a = h\nu_i/c^2$  in order to obtain limits on its coupling. By using the discretized function

$$W(\nu_i, \nu_a, \nu_c) = F(\nu_i) + S_a(\nu_i, \nu_a, \nu_c)B, \quad (12)$$

fits were performed on all 23 subruns. This fit function has  $g_{a\gamma\gamma}^2$  as fitting parameter, in addition to those of  $F(\nu)$  previously described. In order for the fits to converge, the parameters of  $F(\nu)$  have as an initial guess the values found

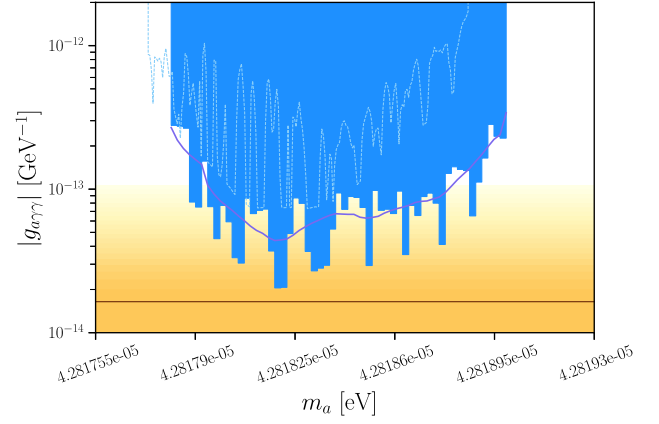


FIG. 7.  $g_{a\gamma\gamma}$  axion coupling constant upper limit calculated with 90% single-sided C.L. as a function of the axion mass. The solid blue bars are the limits obtained with the data and the analysis described in this manuscript. The solid dark blue line is the expected limit in the case of no signal. The dashed light blue line is the limits obtained in our previous work [33]. The yellow region indicates the QCD axion model band. The horizontal line shows the theoretical prediction for the coupling constant given by the Kim-Shifman-Vainshtein-Zakharov (KSVZ) [59,60] model. Image realized with Ref. [61].

when fitting only the background, and they are also constrained to vary in a small interval. We have verified that such a procedure is able to extract the correct value of  $g_{a\gamma\gamma}^2$  by performing Monte Carlo simulations with software injected signals in our data.

The 23 estimated set of values  $g_{a\gamma\gamma}^2(\nu_i)$  are then averaged using as weights the inverse of their squared uncertainties extracted by the fitting procedure. Using this approach, we are able to extract a set of  $g_{a\gamma\gamma}^2$  values from which we calculated the limit on the coupling strength with a 90% confidence level [32], adopting a power constrained procedure for the values of  $g_{a\gamma\gamma}^2$  that fluctuates below  $-\sigma_{g_{a\gamma\gamma}}$  [58]. Because of the nonzero linewidth of the axion and comparing it with the step size, a smoothing effect is expected. Indeed, the observed fluctuations are within one sigma. The upper limits  $g_{a\gamma\gamma}^{\text{C.L.}}$  obtained adopting this procedure in the axion mass range 42.8178 – 42.8190  $\mu\text{eV}$  are reported in Fig. 7 as blue bars. The minimum value sets a limit  $g_{a\gamma\gamma}^{\text{C.L.}} < 2.1 \times 10^{-14} \text{ GeV}^{-1}$ , that is, 1.2 times larger with respect to the benchmark KSVZ axion models [59,60].

#### IV. CONCLUSIONS

We reported results of the search of galactic axions using a high- $Q$  dielectric haloscope instrumented with a detection chain based on a traveling wave parametric amplifier working close to the quantum limit. The investigated mass range is 42.8178 – 42.8190  $\mu\text{eV}$ , partially already investigated by us in a previous run and not currently accessible by other experiments. We set a limit to the axion coupling constant that is about 1.2 times larger with respect to the

benchmark KSVZ axion model. Our results demonstrate the reliability of our approach, which complements high- $Q$  factor dielectric cavities with a strong magnetic field, and operation in an ultracryogenic environment to exploit the noise performances of the TWPA-based detection chain. This is the first time a wide bandwidth quantum limited amplifier has been used in a haloscope working at high frequency, where internal losses of the components are significantly larger with respect to frequencies in the lower octave band, a result that complements the one obtained at 5 GHz by the ADMX Collaboration [62] and paves the road for the exploration of the axion mass parameter space at frequencies above 10 GHz. To fully exploit the TWPA capabilities at such high frequencies, a reduction of its distributed dielectric loss is expected for the future.

This result improves by a factor of about 4 the sensitivity we obtained in our previous run in almost the same frequency range, thanks to the new amplifier and an improved description of the background in the data analysis, based on a robust noise model. With the implementation of antialiasing filters in our digitizing channels and a planned better isolation of the first-stage amplifier, we expect to improve even more our sensitivity in the next run. A new type of cavity with larger effective volume and larger tuning will be put in operation for a future campaign of axion searches capable of covering a sizable range of mass values in the 40  $\mu\text{eV}$  range.

The data that support the findings of this study are available from the corresponding author upon reasonable request.

### ACKNOWLEDGMENTS

We are grateful to E. Berto, A. Benato, and M. Rebeschini for the mechanical work and F. Calaon and M. Tessaro for help with the electronics and cryogenics. We thank G. Galet and L. Castellani for the development of the magnet power supply and M. Zago, who realized the technical drawings of the system. We deeply acknowledge the Cryogenic Service of the Laboratori Nazionali di Legnaro for providing us with large quantities of liquid helium on demand. This work is supported by INFN (QUAX experiment), by the U.S. Department of Energy, Office of Science, National Quantum Information Science Research Centers, Superconducting Quantum Materials and Systems Center (SQMS) under Contract No. DE-AC02-07CH11359, by the European Union’s FET Open SUPERGALAX project, Grant No. 863313, and by the European Union’s Horizon 2020 research and innovation program under Grant Agreement No. 899561. M.E. acknowledges the European Union’s Horizon 2020 research and innovation program under the Marie Skłodowska Curie (Grant Agreement No. MSCA-IF-835791). A. R. acknowledges the European Union’s Horizon 2020 research and innovation program under the Marie Skłodowska Curie Grant Agreement No. 754303 and the “Investissements d’avenir” (ANR-15- IDEX-02) programs of

the French National Research Agency. N. C. is supported by the European Union’s Horizon 2020 research and innovation program under the Marie Skłodowska-Curie Grant Agreement QMET No. 101029189.

### APPENDIX A: DARK PHOTON LIMITS

Following Ref. [63], it is possible to use the limits obtained for the axion to other dark matter candidates such as dark photons (DPs). The DP is the gauge boson of a new dark U(1) added to the standard model (SM) gauge group, under which the SM fields are uncharged: This results in a nearly unobservable DP, except for a small kinetic mixing  $\chi_{\text{DP}}$  with the visible photon that is left in the theory at low energies. To recast a limit on  $g_{\text{a}\gamma\gamma}$  to one on  $\chi_{\text{DP}}$ , one just replaces [63,64]:

$$\chi_{\text{DP}} = g_{\text{a}\gamma\gamma} \frac{B}{m_\chi |\cos \theta|}, \quad (\text{A1})$$

where  $B = 7.1$  T is the rms magnetic field value,  $m_\chi$  is the mass of the dark photon, and  $\cos \theta = \hat{\mathbf{X}} \cdot \hat{\mathbf{B}}$ . The vector  $\hat{\mathbf{X}}$  describes the polarization of the dark photon field.

Two different scenarios have to be considered. For a random polarization scenario and considering that our measurement times were always longer than 1800 s, the value  $\cos \theta = \sqrt{1/3}$  can be used. For a linear polarization scenario, the value of  $\cos \theta$  is averaged over the acquisition time. Distributions of  $\langle \cos^2 \theta \rangle_{T_m}$  are given in Ref. [63] for different positions of the detector vs measurement time  $T_m$ . The QUAX apparatus is a vertical axis haloscope (zenith-pointing) located at a latitude of  $45.35^\circ$  north, and  $\langle \cos^2 \theta \rangle_{T_m}$  values can be obtained from Fig. 5 in Ref. [63]. Figure 8 shows the limits on  $\chi_{\text{DP}}$  obtained for the two DP polarization scenarios from our axion result given in Fig. 7.

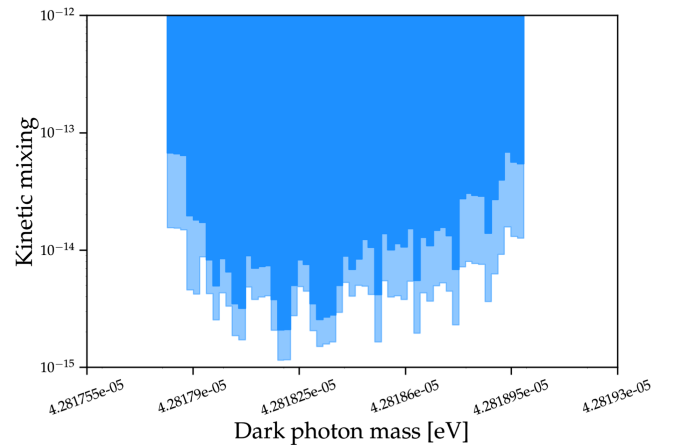


FIG. 8. Dark photon kinetic mixing  $\chi_{\text{DP}}$  upper limit calculated at 90% C.L. as a function of the DP mass. The light blue limits are for the random polarization scenario and the dark blue for the linear polarization scenario. Image realized with Ref. [61].

## APPENDIX B: DETAILS ON THE EXPERIMENTAL SETUP

Table V shows the relevant components used in the experimental setup.

TABLE V. Description of the relevant components for the experimental setup. IL = insertion loss.

Components	Type	Provider or model	Parameters @ 10 GHz
Cryogenic setup—Fig. 1			
K1, K2, K3	Attenuators	Hewlett Packard 8493B 20 DB	IL = 20 dB
C1	Circulator	Raditek RADC-8-12-Cryo-0.02-4K-S23-1WR-MS-b	IL = 0.6 dB
C2, C3	Isolator	Raditek RADI-8-12-Cryo-0.02-4K-S23-1WR-MS-b	IL = 0.6 dB
HP	High-pass filter	Mini Circuit VHF-7150+	IL = 0.7 dB
Cables	rf cable	KeyCom ULT-05	IL = 1.9 dB/m
Cables	SC rf cable	KeyCom NbTiNbTi085	...
HEMT	Amplifier	Low Noise Factory LNF-LNC4-16B	Gain = 42 dB
⊗	Thermometer	ICE Oxford RuO2 RCWPM 1206-68-2.21 KOHM	
$I_{DC}$	Current source	Keithley 263	
Room temperature setup—Fig. 2			
K4	Attenuator	Narda Micro-Pad 4779-12	IL = 12 dB
Cables	rf cable	Huber—Suhner SF104	IL = 1 dB/m
CD1	Power splitter	Macom 1147	
CD2	Power combiner	Triangle Microwave YL—74	
HEMT	Amplifier	Low Noise Factory LNF-LNR4-16B	Gain = 35 dB
AI, AQ	Amplifier	Femto DHPVA-101	Gain (1 MHz) = 50 dB
Mixer	Mixer	Miteq IRM0812LC2Q	...
A1	Amplifier	MITEQ AFS4-08001200-10-CR-4	Gain = 32 dB
Noise source	Noise source	Micronetics NS346B	$T_{eff} = 10000$ K
SG1, SG2, LO, PUMP	Signal generator	Keysight N5183/N5173	
SA	Spectrum analyzer	Keysight N9010B	
ADC	Analog to digital converter	National Instruments USB 6366	Rate = 2 Ms/s
Other components			
Dewar		Precision Cryogenics System Inc.	
Dilution unit		Leiden Cryogenics	
Magnet		Cryogenic Ltd	

- [1] S. Weinberg, A New Light Boson?, *Phys. Rev. Lett.* **40**, 223 (1978).
- [2] F. Wilczek, Problem of Strong  $P$  and  $T$  Invariance in the Presence of Instantons, *Phys. Rev. Lett.* **40**, 279 (1978).
- [3] R. D. Peccei and H. R. Quinn,  $CP$  Conservation in the Presence of Pseudoparticles, *Phys. Rev. Lett.* **38**, 1440 (1977).
- [4] J. Preskill, M. B. Wise, and F. Wilczek, Cosmology of the invisible axion, *Phys. Lett.* **120B**, 127 (1983).
- [5] L. Abbott and P. Sikivie, A cosmological bound on the invisible axion, *Phys. Lett.* **120B**, 133 (1983).
- [6] M. Dine and W. Fischler, The not-so-harmless axion, *Phys. Lett.* **120B**, 137 (1983).
- [7] I. G. Irastorza and J. Redondo, New experimental approaches in the search for axion-like particles, *Prog. Part. Nucl. Phys.* **102**, 89 (2018).
- [8] P. Sikivie, Experimental Tests of the “Invisible” Axion, *Phys. Rev. Lett.* **51**, 1415 (1983).
- [9] P. Sikivie, Detection rates for “invisible”-axion searches, *Phys. Rev. D* **32**, 2988 (1985).
- [10] T. Braine, R. Cervantes, N. Crisosto, N. Du, S. Kimes, L. Rosenberg, G. Rybka, J. Yang, D. Bowring, A. Chou *et al.*, Extended Search for the Invisible Axion with the Axion

- Dark Matter Experiment, *Phys. Rev. Lett.* **124**, 101303 (2020).
- [11] N. Du, N. Force, R. Khatiwada, E. Lentz, R. Ottens, L. Rosenberg, G. Rybka, G. Carosi, N. Woollett, D. Bowring *et al.*, Search for Invisible Axion Dark Matter with the Axion Dark Matter Experiment, *Phys. Rev. Lett.* **120**, 151301 (2018).
- [12] C. Boutan, M. Jones, B. H. LaRoque, N. Oblath, R. Cervantes, N. Du, N. Force, S. Kimes, R. Ottens, L. Rosenberg *et al.*, Piezoelectrically Tuned Multimode Cavity Search for Axion Dark Matter, *Phys. Rev. Lett.* **121**, 261302 (2018).
- [13] C. Bartram *et al.*, Search for Invisible Axion Dark Matter in the 3.3–4.2  $\mu\text{eV}$  Mass Range, *Phys. Rev. Lett.* **127**, 261803 (2021).
- [14] K. M. Backes, D. A. Palken, S. A. Kenany, B. M. Brubaker, S. Cahn, A. Droster, G. C. Hilton, S. Ghosh, H. Jackson, S. K. Lamoreaux *et al.*, A quantum enhanced search for dark matter axions, *Nature (London)* **590**, 238 (2021).
- [15] L. Zhong, S. Al Kenany, K. Backes, B. Brubaker, S. Cahn, G. Carosi, Y. Gurevich, W. Kindel, S. Lamoreaux, K. Lehnert *et al.*, Results from phase 1 of the haystac microwave cavity axion experiment, *Phys. Rev. D* **97**, 092001 (2018).
- [16] M. J. Jewell *et al.* (HAYSTAC Collaboration), New results from haystac’s phase ii operation with a squeezed state receiver, *Phys. Rev. D* **107**, 072007 (2023).
- [17] B. T. McAllister, G. Flower, E. N. Ivanov, M. Goryachev, J. Bourhill, and M. E. Tobar, The organ experiment: An axion haloscope above 15 ghz, *Phys. Dark Universe* **18**, 67 (2017).
- [18] A. Quiskamp, B. T. McAllister, P. Altin, E. N. Ivanov, M. Goryachev, and M. E. Tobar, Direct search for dark matter axions excluding alpogenesis in the 63- to 67- $\mu\text{eV}$  range with the organ experiment, *Sci. Adv.* **8**, eabq3765 (2022).
- [19] J. Choi, S. Ahn, B. Ko, S. Lee, and Y. K. Semertzidis, CAPP-8 TB: Axion dark matter search experiment around 6.7  $\mu\text{eV}$ , *Nucl. Instrum. Methods Phys. Res., Sect. A* **1013**, 165667 (2021).
- [20] S. Lee, S. Ahn, J. Choi, B. Ko, and Y. K. Semertzidis, Axion Dark Matter Search Around 6.7  $\mu\text{eV}$ , *Phys. Rev. Lett.* **124**, 101802 (2020).
- [21] J. Jeong, S. Youn, S. Bae, J. Kim, T. Seong, J. E. Kim, and Y. K. Semertzidis, Search for Invisible Axion Dark Matter with a Multiple-Cell Haloscope, *Phys. Rev. Lett.* **125**, 221302 (2020).
- [22] O. Kwon, D. Lee, W. Chung, D. Ahn, H. Byun, F. Caspers, H. Choi, J. Choi, Y. Chong, H. Jeong *et al.*, First Results from an Axion Haloscope at CAPP Around 10.7  $\mu\text{eV}$ , *Phys. Rev. Lett.* **126**, 191802 (2021).
- [23] Y. Lee, B. Yang, H. Yoon, M. Ahn, H. Park, B. Min, D. Kim, and J. Yoo, Searching for Invisible Axion Dark Matter with an 18 T Magnet Haloscope, *Phys. Rev. Lett.* **128**, 241805 (2022).
- [24] C. M. Adair *et al.*, Search for dark matter axions with CAST-CAPP, *Nat. Commun.* **13**, 6180 (2022).
- [25] A. K. Yi *et al.*, Axion Dark Matter Search Around 4.55  $\mu\text{eV}$  with Dine-Fischler-Srednicki-Zhitnitskii Sensitivity, *Phys. Rev. Lett.* **130**, 071002 (2023).
- [26] T. Grenet, R. Ballou, Q. Basto, K. Martineau, P. Perrier, P. Pugat, J. Quevillon, N. Roch, and C. Smith, The grenoble axion haloscope platform (GrAHal): Development plan and first results, [arXiv:2110.14406](https://arxiv.org/abs/2110.14406).
- [27] A. Á. Melcón, S. A. Cuendis, C. Cogollos, A. Díaz-Morcillo, B. Döbrich, J. D. Gallego, J. Barceló, B. Gimeno, J. Golm, I. G. Irastorza *et al.*, Scalable haloscopes for axion dark matter detection in the 30  $\mu\text{eV}$  range with rades, *J. High Energy Phys.* **07** (2020) 084.
- [28] A. A. Melcon, S. A. Cuendis, C. Cogollos, A. Díaz-Morcillo, B. Döbrich, J. D. Gallego, B. Gimeno, I. G. Irastorza, A. J. Lozano-Guerrero, C. Malbrunot *et al.*, Axion searches with microwave filters: The rades project, *J. Cosmol. Astropart. Phys.* **05** (2018) 040.
- [29] A. Álvarez Melcón, S. Arguedas Cuendis, J. Baier, K. Barth, H. Bräuninger, S. Calatroni, G. Cantatore, F. Caspers, J. Castel, S. A. Cetin *et al.*, First results of the cast-rades haloscope search for axions at 34.67  $\mu\text{eV}$ , *J. High Energy Phys.* **10** (2021) 075.
- [30] H. Chang, J.-Y. Chang, Y.-C. Chang, Y.-H. Chang, Y.-H. Chang, C.-H. Chen, C.-F. Chen, K.-Y. Chen, Y.-F. Chen, W.-Y. Chiang, W.-C. Chien, H. T. Doan, W.-C. Hung, W. Kuo, S.-B. Lai, H.-W. Liu, M.-W. OuYang, P.-I. Wu, and S.-S. Yu (TASEH Collaboration), Taiwan axion search experiment with haloscope: Cd102 analysis details, *Phys. Rev. D* **106**, 052002 (2022).
- [31] D. Alesini, C. Braggio, G. Carugno, N. Crescini, D. D’Agostino, D. Di Gioacchino, R. Di Vora, P. Falferi, S. Gallo, U. Gambardella *et al.*, Galactic axions search with a superconducting resonant cavity, *Phys. Rev. D* **99**, 101101 (2019).
- [32] D. Alesini, C. Braggio, G. Carugno, N. Crescini, D. D’Agostino, D. Di Gioacchino, R. Di Vora, P. Falferi, U. Gambardella, C. Gatti *et al.*, Search for invisible axion dark matter of mass  $m_a = 43 \mu\text{eV}$  with the quax- $\gamma$  experiment, *Phys. Rev. D* **103**, 102004 (2021).
- [33] D. Alesini, D. Babusci, C. Braggio, G. Carugno, N. Crescini, D. D’Agostino, A. D’Elia, D. Di Gioacchino, R. Di Vora, P. Falferi, U. Gambardella, C. Gatti, G. Iannone, C. Ligi, A. Lombardi, G. Maccarrone, A. Ortolan, R. Pengo, A. Rettaroli, G. Ruoso, L. Taffarello, and S. Tocci, Search for galactic axions with a high- $q$  dielectric cavity, *Phys. Rev. D* **106**, 052007 (2022).
- [34] R. Barbieri, C. Braggio, G. Carugno, C. S. Gallo, A. Lombardi, A. Ortolan, R. Pengo, G. Ruoso, and C. C. Speake, Searching for galactic axions through magnetized media: The quax proposal, *Phys. Dark Universe* **15**, 135 (2017).
- [35] N. Crescini, D. Alesini, C. Braggio, G. Carugno, D. Di Gioacchino, C. S. Gallo, U. Gambardella, C. Gatti, G. Iannone, G. Lamanna *et al.*, Operation of a ferromagnetic axion haloscope at  $m_a = 58 \mu\text{eV}$ , *Eur. Phys. J. C* **78**, 703 (2018).
- [36] N. Crescini, D. Alesini, C. Braggio, G. Carugno, D. D’Agostino, D. Di Gioacchino, P. Falferi, U. Gambardella, C. Gatti, G. Iannone *et al.*, Axion Search with a Quantum-Limited Ferromagnetic Haloscope, *Phys. Rev. Lett.* **124**, 171801 (2020).
- [37] C. Gatti, D. Alesini, D. Babusci, C. Braggio, G. Carugno, N. Crescini, D. Di Gioacchino, P. Falferi, G. Lamanna, C. Ligi *et al.*, The klash proposal: Status and perspectives, [arXiv:1811.06754](https://arxiv.org/abs/1811.06754).

- [38] D. Alesini, D. Babusci, F. Björkeröth, F. Bossi, P. Ciambrone, G. D. Monache, D. Di Gioacchino, P. Falferi, A. Gallo, C. Gatti *et al.*, Klash conceptual design report, [arXiv:1911.02427](https://arxiv.org/abs/1911.02427).
- [39] A. Caldwell, G. Dvali, B. Majorovits, A. Millar, G. Raffelt, J. Redondo, O. Reimann, F. Simon, and F. Steffen (MADMAX Working Group), Dielectric Haloscopes: A New Way to Detect Axion Dark Matter, *Phys. Rev. Lett.* **118**, 091801 (2017).
- [40] S. Knirck *et al.* (The MADMAX Collaboration), Simulating madmax in 3d: Requirements for dielectric axion haloscopes, *J. Cosmol. Astropart. Phys.* **10** (2021) 034.
- [41] M. Lawson, A. J. Millar, M. Pancaldi, E. Vitagliano, and F. Wilczek, Tunable Axion Plasma Haloscopes, *Phys. Rev. Lett.* **123**, 141802 (2019).
- [42] A. J. Millar *et al.* (Endorsers Collaboration), Searching for dark matter with plasma haloscopes, *Phys. Rev. D* **107**, 055013 (2023).
- [43] S. Al Kenany, M. Anil, K. Backes, B. Brubaker, S. Cahn, G. Carosi, Y. Gurevich, W. Kindel, S. Lamoreaux, K. Lehnert *et al.*, Design and operational experience of a microwave cavity axion detector for the 20 – 100  $\mu\text{eV}$  range, *Nucl. Instrum. Methods Phys. Res., Sect. A* **854**, 11 (2017).
- [44] D. Di Gioacchino, C. Gatti, D. Alesini, C. Ligi, S. Tocci, A. Rettaroli, G. Carugno, N. Crescini, G. Ruoso, C. Braggio *et al.*, Microwave losses in a dc magnetic field in superconducting cavities for axion studies, *IEEE Trans. Appl. Supercond.* **29**, 1 (2019).
- [45] D. Ahn, O. Kwon, W. Chung, W. Jang, D. Lee, J. Lee, S. W. Youn, D. Youm, and Y. K. Semertzidis, Maintaining high q-factor of superconducting  $\text{YBa}_2\text{Cu}_3\text{O}_{7-x}$  microwave cavity in a high magnetic field, [arXiv:1904.05111](https://arxiv.org/abs/1904.05111).
- [46] D. Alesini, C. Braggio, G. Carugno, N. Crescini, D. D’Agostino, D. Di Gioacchino, R. Di Vora, P. Falferi, U. Gambardella, C. Gatti *et al.*, High quality factor photonic cavity for dark matter axion searches, *Rev. Sci. Instrum.* **91**, 094701 (2020).
- [47] D. Alesini, C. Braggio, G. Carugno, N. Crescini, D. D’Agostino, D. Di Gioacchino, R. Di Vora, P. Falferi, U. Gambardella, C. Gatti *et al.*, Realization of a high quality factor resonator with hollow dielectric cylinders for axion searches, *Nucl. Instrum. Methods Phys. Res., Sect. A* **985**, 164641 (2021).
- [48] R. Di Vora, D. Alesini, C. Braggio, G. Carugno, N. Crescini, D. D’Agostino, D. Di Gioacchino, P. Falferi, U. Gambardella, C. Gatti, G. Iannone, C. Ligi, A. Lombardi, G. Maccarrone, A. Ortolan, R. Pengo, A. Rettaroli, G. Ruoso, L. Taffarello, and S. Tocci, High- $q$  Microwave Dielectric Resonator for Axion Dark-Matter Haloscopes, *Phys. Rev. Appl.* **17**, 054013 (2022).
- [49] A. Ranadive, M. Esposito, L. Planat, E. Bonet, C. Naud, O. Buisson, W. Guichard, and N. Roch, Kerr reversal in Josephson meta-material and traveling wave parametric amplification, *Nat. Commun.* **13**, 1737 (2022).
- [50] A. Marin, M. Bignotto, M. Bonaldi, M. Cerdonio, P. Falferi, R. Mezzena, G. A. Prodi, G. Soranzo, L. Taffarello, A. Vinante, S. Vitale, and J.-P. Zendri, Noise measurements and optimization of the high sensitivity capacitive transducer of AURIGA, *Classical Quantum Gravity* **19**, 1991 (2002).
- [51] C. Braggio, G. Cappelli, G. Carugno, N. Crescini, R. D. Vora, M. Esposito, A. Ortolan, L. Planat, A. Ranadive, N. Roch, and G. Ruoso, A haloscope amplification chain based on a traveling wave parametric amplifier, *Rev. Sci. Instrum.* **93**, 094701 (2022).
- [52] L. Planat, E. Al-Tavil, J. P. Martínez, R. Dassonneville, F. Foroughi, S. Léger, K. Bharadwaj, J. Delaforce, V. Milchakov, C. Naud, O. Buisson, W. Hasch-Guichard, and N. Roch, Fabrication and Characterization of Aluminum Squid Transmission Lines, *Phys. Rev. Appl.* **12**, 064017 (2019).
- [53] M. S. Turner, Periodic signatures for the detection of cosmic axions, *Phys. Rev. D* **42**, 3572 (1990).
- [54] M. S. Bartlett, Smoothing periodograms from time-series with continuous spectra, *Nature (London)* **161**, 686 (1948).
- [55] L. Di Luzio, M. Giannotti, E. Nardi, and L. Visinelli, The landscape of QCD axion models, *Phys. Rep.* **870**, 1 (2020).
- [56] B. M. Brubaker, L. Zhong, S. K. Lamoreaux, K. W. Lehnert, and K. A. van Bibber, Haystack axion search analysis procedure, *Phys. Rev. D* **96**, 123008 (2017).
- [57] P. A. Zyla *et al.* (Particle Data Group), Review of particle physics, *Prog. Theor. Exp. Phys.* **2020**, 083C01 (2020).
- [58] G. Cowan, K. Cranmer, E. Gross, and O. Vitells, Power-constrained limits, [arXiv:1105.3166](https://arxiv.org/abs/1105.3166).
- [59] J. E. Kim, Weak-Interaction Singlet and Strong  $CP$  Invariance, *Phys. Rev. Lett.* **43**, 103 (1979).
- [60] M. Shifman, A. Vainshtein, and V. Zakharov, Can confinement ensure natural  $CP$  invariance of strong interactions?, *Nucl. Phys.* **B166**, 493 (1980).
- [61] C. O’Hare, cajohare/axionlimits: Axionlimits, <https://cajohare.github.io/AxionLimits/> (2020).
- [62] C. Bartram *et al.*, Dark matter axion search using a Josephson traveling wave parametric amplifier, *Rev. Sci. Instrum.* **94**, 044703 (2023).
- [63] A. Caputo, A. J. Millar, C. A. J. O’Hare, and E. Vitagliano, Dark photon limits: A handbook, *Phys. Rev. D* **104**, 095029 (2021).
- [64] P. Arias, D. Cadamuro, M. Goodsell, J. Jaeckel, J. Redondo, and A. Ringwald, Wispy cold dark matter, *J. Cosmol. Astropart. Phys.* **06** (2012) 013.